Environmental Science: Atmospheres

ROYAL SOCIETY OF CHEMISTRY

PAPER

View Article Online
View Journal

Cite this: DOI: 10.1039/d5ea00145e

Oxidation of organic films at the mineral–water interface by aqueous-phase ozone affects aerosol light scattering

Edward J. Stuckey, [ab] Rebecca J. L. Welbourn, [bc] Tobias W. D. Robson, [ad] Philipp Gutfreund, [e] Katherine C. Thompson, [f] Adrian R. Rennie [g] and Martin D. King *[a]

Interfacial organic films on atmospheric aerosol particulates can modify their light scattering properties, potentially impacting Earth's radiative balance. Here, a proxy for organic films at the aerosol mineral–water interface is measured using neutron reflectometry, and the results are contextualized in a single particle light scattering model, N-Mie. Model lipid-bilayers, composed of DPPC (no double bonds), POPC (1 carbon–carbon double bond), and DOPC (2 carbon–carbon double bonds), were deposited on a silica–water interface and oxidized with aqueous ozone to simulate the oxidation of organic films on aqueous mineral aerosol particles. Neutron reflectometry measurements showed that these bilayers initially formed films approximately 4 nm thick, and oxidation by aqueous ozone led to thickness reductions proportional to the number of carbon–carbon double bonds. Post-oxidation thicknesses were 4 nm (DPPC), 1.6 nm (POPC), and 0.4 nm (DOPC). Light scattering modelling of particulates with a mineral core and water film revealed that a 1 nm lipid-like organic film at the mineral–water interface had similar effects on the single scattering albedo (ω) asymmetry parameter (g), and forcing efficiency $\left(\frac{\Delta F}{\tau}\right)$ of an aerosol particulate as at the air–water interface. The Mie modelling also revealed that an increase in the thickness of the organic film at the mineral–water interface of up to 10 nm results in an increase in forward scattering of light ($\Delta g = 0.025$), a decrease in the amount of light scattered ($\Delta\omega = -0.016$) and an aerosol forcing efficiency $\left(\Delta\frac{\Delta F}{\tau} = 0.009\ \mathrm{W\ m^{-2}}\right)$. The findings presented here indicate that organic films with experimentally measured thicknesses at the mineral–water interface can significantly alter aerosol forcing efficiency.

Received 4th November 2025
Accepted 21st April 2026

DOI: 10.1039/d5ea00145e

rsc.li/esatmospheres

Environmental significance

Atmospheric aerosols influence Earth's climate by scattering and absorbing sunlight, yet the role of organic films at aerosol interfaces remains poorly constrained. Understanding how these interfacial layers modify light scattering is essential for accurately representing aerosol–radiation interactions in climate models. The work presented here combines neutron reflectometry with light-scattering simulations to quantify how ozone oxidation alters the thickness and optical effects of lipid-like organic films on aqueous mineral surfaces. The results show that film oxidation markedly influence scattering properties and aerosol forcing efficiency. These findings demonstrate that nanometer scale interfacial organic layers, commonly present on atmospheric particles, can meaningfully affect radiative forcing, emphasizing the need to include interfacial chemistry in climate-relevant aerosol models.

[a]Department of Earth Sciences, Royal Holloway University of London, Egham, Surrey TW20 0EX, UK. E-mail: m.king@rhul.ac.uk
[b]ISIS Neutron & Muon Source, Rutherford Appleton Laboratory, Didcot, Oxfordshire OX11 0QX, UK
[c]Oak Ridge National Laboratory, 1 Bethel Valley Road, Oak Ridge, TN 37830, USA
[d]Forestry Research, Alice Holt Lodge, Wrecclesham, Farnham, GU10 4LH, UK
[e]Institut Laue-Langevin, 71 Avenue des Martyrs, CS 20156, 38042 Grenoble Cedex 9, France
[f]School of Natural Sciences, Birkbeck, University of London, Malet Street, London WC1E 7HX, UK
[g]Department of Chemistry, Ångström Laboratory, Uppsala University, Lägerhyddsvägen 1, Box 538, 751 21 Uppsala, Sweden

1 Introduction

Organic thin films can form at the air–water interface of aqueous atmospheric aerosol and hydrometeors and have been shown to have significant atmospheric impacts,[1–6] altering the light scattering and cloud-water nucleating potential of atmospheric aerosol.[1,2,4,7–9] In prior studies, the authors of the work presented here have shown that there are significant and similar light scattering effects on atmospheric aerosol owing to the presence of thin films of the same thicknesses at the air–

water[10,11] and mineral–air interface.[12] However, the importance of organic thin films at the alternative, but linked, mineral–water interface of the aerosol remains relatively unknown. A simplistic representation of atmospheric aerosol with films at the "air–water" and "mineral–water" interfaces are provided in Fig. 1. Here, the authors undertake a combination of experimental measurements and single particle Mie scattering modelling to better understand the atmospheric importance of organic thin films at the aerosol mineral–water interface.

A significant proportion of atmospheric aerosol is comprised of mineral material, with mineral dust contributions to global aerosol emissions reaching an estimated 1000–3000 Mt per year;[13] constituting more than half of the total global aerosol burden.[14–16] Mineral aerosols can affect the atmosphere by scattering and absorbing light,[17–20] by serving as cloud condensation nuclei,[20–23] and by providing a solid surface for chemistry in the atmosphere.[24–27] The atmospheric impact of mineral aerosol is determined in part by their chemical and morphological properties,[14,20,28,29] which may vary spatially, and temporally.[8,30–35] The size distribution of these particles is typically characterized by a multi-modal log-normal distribution by particle radius; while the largest number densities are concentrated in the sub-micron "accumulation mode" ($D_p < 1$ μm), the vast majority of the mass density is sequestered within the coarse mode, often exceeding 10 μm in diameter near source regions.[36] Beyond its physical presence, dust serves as a critical heterogeneous reaction site for atmospheric chemistry, facilitating the uptake and partitioning of trace gases.[27] For laboratory-based kinetic and optical studies, silica (SiO_2) is frequently employed as a robust proxy for natural dust due to its dominance as a primary mineralogical constituent (averaging approximately 60% by mass in crustal samples) and its well-defined surface hydroxyl groups which mimic the reactive behaviour of authentic desert aerosols.[36–38] Owing to the substantial amount of mineral aerosol particulates in the atmosphere, quantifying how they may change over their lifetime is important for refining climate, aerosol, and cloud processing models. One way in which a mineral aerosol may change with time is through the accumulation of organic material at the interfaces of the host particulate as a thin film.[1,39,40] Interfacial organic thin films have been shown to be susceptible to oxidation.[9,41–46] The oxidation of interfacial thin films can alter the optical and hygroscopic properties of the host aerosol particulate, leading to subsequent effects on the weather and climate.[9–12,47,48]

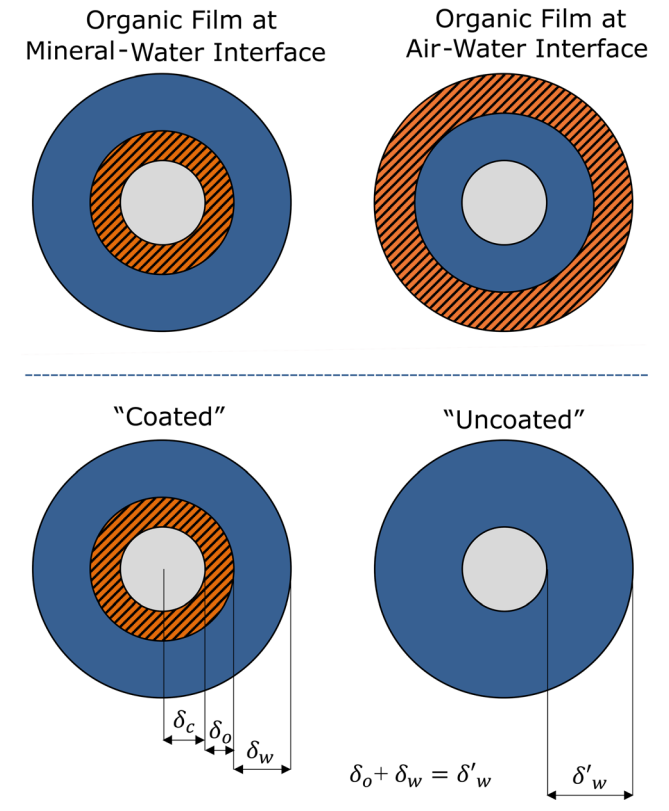

Fig. 1 A schematic of mineral aerosol particles encapsulated by water with an organic film at the mineral–water (top-left) and air–water (top-right) interfaces, and a schematic representation of the core–shell model of the aerosol used in the N-Mie program to calculate the change in single scattering albedo and asymmetry parameter of the aerosol owing to the presence of the organic film discussed later in Sections 2.4, 3.3 and 4.2. The grey/light component represents the mineral core, the blue/dark component represents the water around the particle, and the orange striped layer represents the organic film.

One prevalent oxidant in the atmosphere is ozone. Many molecules in the atmosphere are susceptible to chemical transformation by ozone through reaction pathways such as the addition of oxygen to the carbon–carbon double bond of alkenes[49–52] and triple bonds of alkynes,[52,53] the addition to aromatic rings,[52,54,55] and the oxidation of nitrogen oxides[52,56,57] and sulfides.[52,55] Furthermore, ozone is readily soluble in water,[58,59] which allows aqueous-phase reactions to occur in bulk water.[60,61] Ozone resides in the atmosphere at approximate background concentrations of 30–40 ppb in the gas-phase,[62] and approximately 30 ppb in the aqueous phase, dissolved in atmospheric water,[63] with some spatial and temporal variation in the atmospheric concentrations of ozone across the Earth.[64] Owing to the relatively large concentrations of ozone in the atmosphere, the numerous reaction pathways, and its aqueous solubility, ozone is particularly relevant for the study of thin-film oxidation reactions at atmospheric aerosol interfaces.

Some of the methods of characterizing the chemical and physical properties of films at aerosol and aerosol proxy interfaces include spectrometry,[65–72] spectroscopy,[73–77] chromatography,[78–80] surface tensiometry,[81–83] neutron and X-ray scattering,[10,11,42,48,84–92] and microscopy.[93–95] Despite extensive research into the aerosol air–liquid, liquid–liquid, and solid–air interfaces,[2,3,10,11,41,42,48,73,84–86,88,91,92,96–104] little research has been done on the role of atmospheric organics at the solid–liquid interface, in part due to the complexity of measuring "buried" interfaces. Neutron reflectometry is one technique that enables the observation of buried interfaces[105–107] owing to the ability for neutrons to penetrate certain materials, and has been successfully used elsewhere to investigate organics at the solid–liquid interface and an overview of the recent and historic use of neutron reflectometry to measure the solid–liquid interface can be found in the reviews by Welbourn and Clarke[105] and

Fragneto-Cusani[108] respectively. While neutron reflectometry is well adopted in fields such as biochemistry and soft matter, it remains a novel measurement technique for atmospheric sciences. Neutron reflectometry is the chosen measurement technique for the work presented here owing to its non-destructive, penetrative surface measurement capabilities, and, so far as the authors are aware, the work herein is the first application of neutron reflectometry to consider the atmospheric implications of organic films at the aerosol mineral–water interface.

For this initial investigation into the atmospheric significance of organic thin films at the mineral–water interface, phosphocholine lipids have been used as an atmospheric organic film proxy owing to their ability to self assemble into reproducible organic films at the mineral–water interface.[109] The selected atmospheric proxies for this work are DPPC (1,2-dipalmitoylphosphatidylcholine), POPC (1-palmitoyl-2-oleoyl-*sn*-glycero-3-phosphocholine), and DOPC (1,2-dioleoyl-*sn*-glycero-3-phosphocholine), chosen for their similar molecular structure and varying number of unsaturated carbon–carbon double bonds (0, 1, and 2 respectively). The chemical structure of DPPC, POPC, and DOPC is provided in Fig. 2. The compositional and structural similarities of DPPC, POPC, and DOPC allow for consideration of the significance of the number of unsaturated carbon–carbon double bonds in the extent and duration of organic film oxidation.

Virkkula *et al.*[110] reported that aerosol samples collected in the Eastern Mediterranean contained three main phospholipid classes: phosphatidylcholines (present in 73% of samples), followed by phosphatidylglycerols (20%) and phosphatidylethanolamines (7%). Griffen *et al.*[111] suggested that dust and soil aerosols provide effective surfaces for biological material, including cellular and fungal debris as well as pollen. The lysis of such biological material has been identified as a potential source of phosphocholine lipids.[112,113] Van Acker *et al.*[114] reported the presence of the phosphocholine lipid dipalmitoylphosphatidylcholine (DPPC) in sea spray aerosol in Belgium, with median and maximum air concentrations of 7.1 and 33 pg m^{-3}, respectively. Decesari *et al.*[115] also provided tentative evidence for the presence of phosphocholine lipids in aerosols from the Southern Ocean. More broadly, sea spray aerosol is recognised as a significant source of organic biological material in the atmosphere,[116–118] and that some of this material will form films at the air–water interface.[10,11,86]

The questions this study aims to answer are threefold: what are the thicknesses of films formed by cellular (lipid) material, to what extent are these films removed by exposure to ozone; and, lastly, what are the light scattering impacts of the presence and oxidation of the experimentally measured films on atmospheric aerosol?

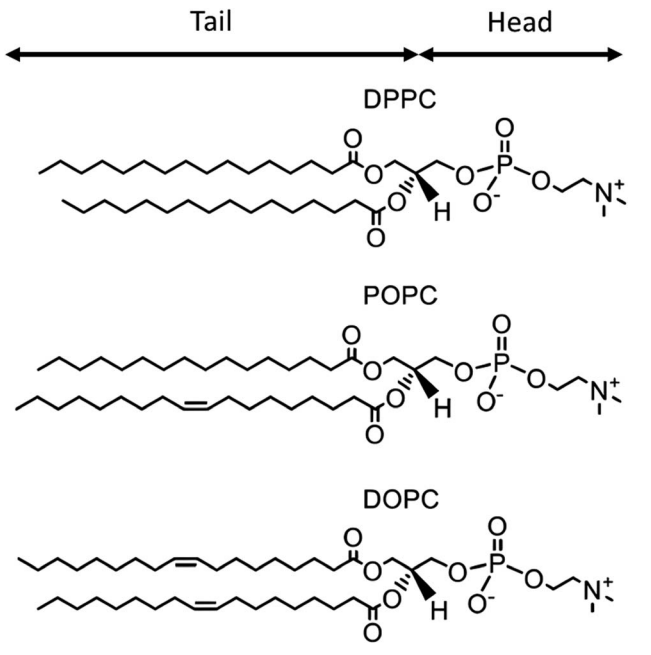

Fig. 2 Diagrams of the chemical structure of the three lipids used in this work, 1,2-dipalmitoylphosphatidylcholine (DPPC), 1-palmitoyl-2-oleoyl-*sn*-glycero-3-phosphocholine (POPC), and 1,2-dioleoyl-*sn*-glycero-3-phosphocholine (DOPC). Diagrams adapted from relevant chemical diagrams at Sigma-Aldrich.

2 Methods

The work presented here employs neutron reflectometry, a surface measurement technique, to analyze thin films at the mineral–water interface as a proxy for similar interfaces in atmospheric aerosols. The thickness of thin films before, during, and after oxidation are incorporated into single-particle Mie scattering models to evaluate the atmospheric significance of these films over an atmospheric aerosol's physical lifetime. From the results of the Mie scattering model, the aerosol forcing efficiency is estimated.

2.1 Neutron reflectometry

Neutron reflectometry is a surface measurement technique that can derive the thickness, inter-layer roughness, and density of a sample at an interface by measurement of the intensity of a beam of specularly reflected neutrons before, I_0, and after, I, interacting with a surface, or "sample". The reflectivity is then the proportion of the incident beam reflected by the sample, as demonstrated in eqn (1).

$$R(Q) = \frac{I}{I_0} \tag{1}$$

The reflectivity is a function of both neutron wavelength, λ_n, and angle of incidence, θ, so the momentum transfer, Q, is used to combine these dependencies as defined in eqn (2). A plot of the reflectivity *versus* momentum transfer is known as the reflectivity profile.

$$Q = \frac{4\pi \sin(\theta)}{\lambda_n} \tag{2}$$

The intensity of the scattering interaction of a neutron with an atom is described by the square of the neutron scattering

length, b. For larger materials composed of multiple atoms the average scattering effect per unit volume, known as the scattering length density, ρ, can be calculated as the sum of the scattering lengths of all atoms within the material divided by their collective volume, V_n, as shown in eqn (3).

$$\rho = \frac{\sum_{i=1}^{N} b_i}{V_n} \quad (3)$$

A comparison of the scattering length densities of an uncoated surface and a surface with a lipid bilayer on, and the reflectivities produced by these, is demonstrated in Fig. 3.

The neutron scattering length of a material is isotopically variable; hence, isotopic substitution can be employed to modify the neutron contrast, effectively masking or enhancing information about certain parts of a sample. In this study, isotopic substitution is utilized to match the neutron scattering length density of water to that of silicon by mixing H_2O and D_2O, thereby isolating information about the lipid bilayer—this solution is referred to as silicon contrast-matched water (SiMW).

The reflectivity measurements in the work presented here[120–124] were made at the ISIS Neutron and Muon Source, UK, using the multi-wavelength instrument INTER,[125–127] with preliminary measurements performed at the Institut Laue-Langevin, France. The data were reduced following standard reduction procedures.[128,129] The high-flux of INTER[125–127] provides a relatively fine time resolution and was used here to monitor the oxidation of organic thin films at the mineral–water interface by aqueous ozone. Throughout the measurements presented here, the neutron footprint was maintained within the sample area of the solid–liquid cell and a constant $\delta q/q$ resolution of 0.03 was controlled using the incident slits. Two incident angles of 0.7° and 2.3° were used to measure over a momentum transfer range between 0.01–0.3 Å^{-1}.

2.2 Reflectometry data analysis

In order to determine the structure of a film at an interface from neutron reflectometry data, a model is required owing to a phenomena known as "the phase problem".[130] Instead of using the reflectivity directly, a model of the scattering length density profile (scattering length density as a function of the distance normal to the interface) is optimized until it most accurately reproduces a measured reflectivity profile, an example of this is shown in Fig. 3. Models of neutron reflectometry data typically consist of a series of uniform slabs between two infinitely thick bulk materials of given values of scattering length density. Each slab is usually parametrized by a thickness, scattering length density, and interlayer roughness. For solid–liquid experiments, the infinite bulk materials are the liquid subphase and the solid substrate.

The work described here has used the Abelès method[131] through the fitting package Refnx.[119] Model scattering length density profiles were parameterized by a set of five slabs

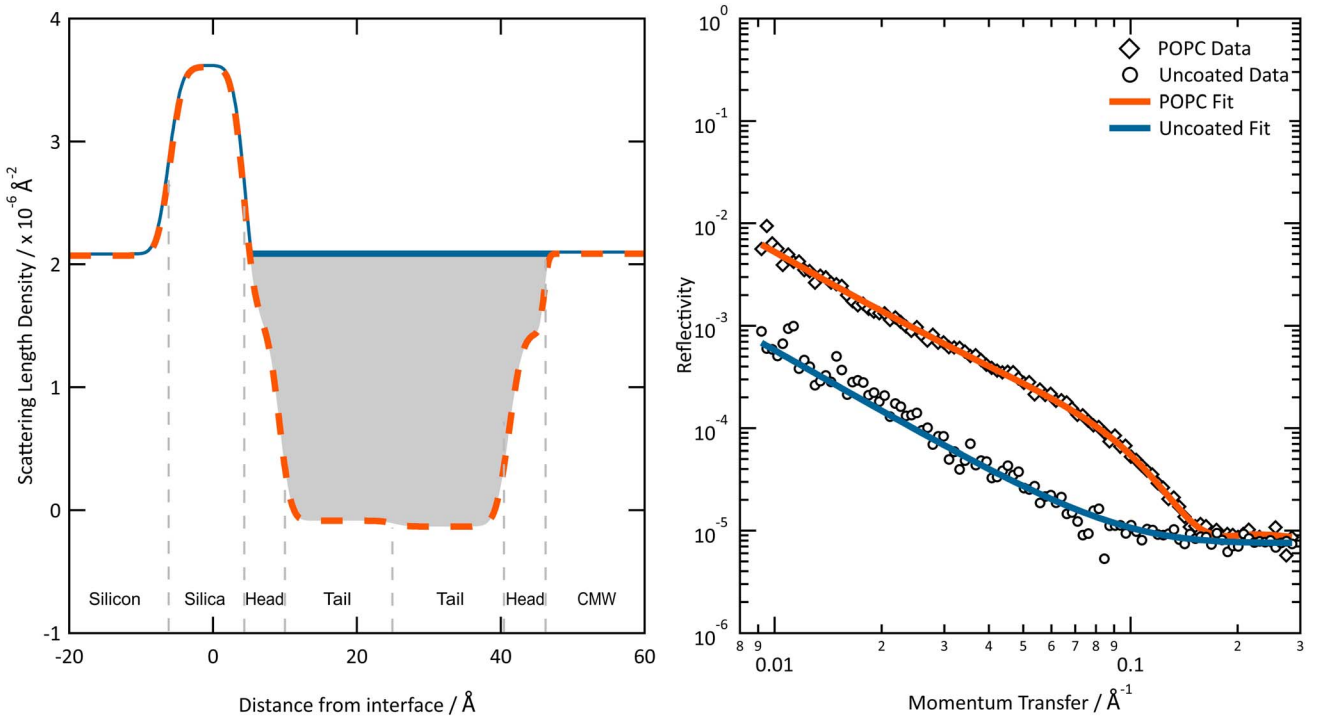

Fig. 3 The neutron scattering length density (left) and reflectivity (right) profiles of an uncoated and POPC lipid bilayer coated silica surface. The best fits shown were produced using the Abelès method in Refnx.[119] Common parameters are used to describe the silica layer and bulk components. The shaded area, the area between the scattering length density profile of the uncoated surface and the surface with a POPC Bilayer, was used to determine the proportion of material remaining at the interface.

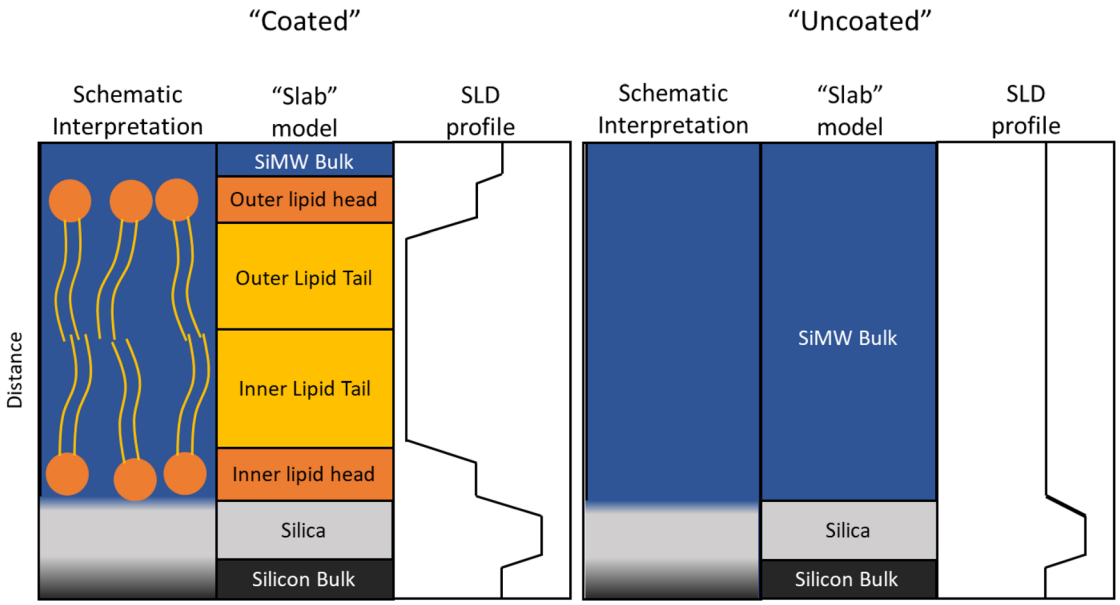

Fig. 4 A simplified representation of a diagram, 'slab' model, and simplified scattering length density profile of a mineral–water interface with and without a lipid bilayer, *i.e.* "coated" and "uncoated".

consisting of the native oxide layer on the silicon, and the head and tail regions of both lipid bilayer leaflets, all between bulk scattering length densities of silicon and the relevant aqueous contrast. A schematic diagram of this is shown in Fig. 4. The scattering length density, thickness, solvation, and interfacial roughness of the lipid components, as well as the thickness and roughness of the oxide layer, were variable parameters. The initial values of the pre-fit parameters were determined from existing literature for the lipid components,[132] and the values of the scattering length density of the bulk and silica layer were determined from the NIST Scattering Length Density Calculator, with the fitting bounds constrained by reasonable physical limitations. For the measurements of the uncoated interface and the lipid bilayers before oxidation, contrasts of the sample with H_2O, D_2O, and SiMW were combined in a co-fitting approach, allowing the values of thickness, interlayer roughness, scattering length densities, and solvation to be retained between the models of each contrast while varying the bulk aqueous phase scattering length density, thereby improving confidence in the fit. To fit the data during the ozonolysis reaction, the scattering length density and thickness of the lipid components were allowed to vary with all other model parameters held at the pre-reaction values. In order to account for the possibility of complete removal of the film, the lipid thickness lower bound was set to zero and the lipid scattering length densities were allowed to vary up to the scattering length density of the subphase.

2.3 Experimental setup & sample preparation

The lipids DPPC, POPC, and DOPC, obtained from Sigma-Aldrich, were dissolved in ultrapure (≥99.9) chloroform at a concentration of 1 mg mL^{-1} and stored in amber glass vials at −18 °C in the dark until experimental use. A maximum of 90 minutes prior to measurement, 1 mL of the lipid-chloroform solution was transferred into an amber glass vial, dried gently under nitrogen, and then combined with ultrapure MilliQ water (>18 MΩ cm) and vigorously shaken until a cloudy appearance was achieved. The resulting water–lipid suspension was sonicated using an ultratip sonicator, employing 10-second pulses for 2 minutes to produce lipid vesicles suspended in a water solution (1 mg mL^{-1}). Vesicle formation was evident from the appearance of a transparent solution with a characteristic faint blue tinge when held up to a light source.

Single-crystal silicon substrates, oriented along the (001) plane, were obtained from and polished by Crystech to a root-mean-square surface roughness of approximately 2 Å. The surface flatness was <5 μm, and the parallelism was maintained within ~0.05°. The crystals were thoroughly washed with water, ethanol, and sulfuric acid, then rinsed with water and cleaned in a UV-Ozone Cleaner for 20 minutes, followed by another rinse with water to ensure they were hydrophilic. The blocks were mounted in solid–liquid cells and measured by neutron reflection under three contrasts: H_2O, D_2O, and SiMW. Lipids were subsequently deposited *via* vesicle fusion, a widely adopted procedure, where, on contact with the solid interface, the vesicles rupture and self-assemble into bilayers. POPC and DOPC were injected at room temperature, whereas DPPC was heated to 50 °C for deposition.[133] The initial state of each bilayer film was measured under D_2O, H_2O, and SiMW contrasts. The ozonolysis reaction was carried out by flowing silicon contrast-matched water containing known concentrations of aqueous ozone continuously through the cell. All fluid exchanges were performed at a rate of 0.5 mL min^{-1}, regulated with a Jasco HPLC pump with the de-gasser bypassed.

The aqueous solutions containing dissolved ozone were prepared by passing gaseous oxygen through a corona discharge

ozonizer at a rate of 0.005 L min^{-1} to generate gas-phase ozone at mixing ratios exceeding 1000 ppm, which was then bubbled into 200 mL of silicon contrast-matched water whilst stirring. The concentration of ozone in the water did not increase beyond 2 hours, plateauing at a concentration of approximately 42 μmol dm^{-3}, as determined by UV-vis spectroscopy[134] using the absorbance at 260 nm and a molar absorption coefficient of 2992 M^{-1} L cm^{-1}.[135] Dilutions of 1 : 4 v/v (8.3 μmol dm^{-3}) and 1 : 19 (2.1 μmol dm^{-3}) were prepared and kept in amber bottles in the dark at 4 °C, with a single drop of concentrated sulfuric acid added to each 1 L solution (pH ~1) to prevent decay.[136] Aqueous ozone solutions were prepared a maximum of 2 hours before use.

2.4 Mie scattering

Mie scattering is the dominant form of light scattering caused by aerosols in the atmosphere owing to the similarity of their size and the wavelength of sunlight,[33,137,138] and is the focus of a wide range of atmospheric[33,137,139] and astronomical[140–142] research. Despite atmospheric aerosol comprising a variety of complex particle shapes, it is common to approximate the aerosol particles to homogeneous spheres. Typically the aerosol particles are described as one or more concentric spheres with given refractive indices,[143] and an equivalent approach is used herein.

The atmospheric aerosol considered in the work presented here consist of three components, a mineral core (silica), surrounded by layers of organic (*e.g.* lipid-like) material and water, and hence are considered as a "multi-layered sphere", as depicted in Fig. 1. To calculate the optical properties of a multi-layered sphere, the Mie scattering program N-Mie by Voshchinnikov *et al.*,[144] based on the recursive algorithms by Wu and Wang,[145] is implemented. N-Mie represents multi-layered spheres as a series of concentric spheres, each with a given radius/thickness and complex refractive index. N-Mie has been used extensively elsewhere, including to determine the effect of thin films on aerosol optical properties.[110] The Mie scattering analysis in this work focuses primarily on changes in film thickness rather than chemical composition as the refractive index of the organic material is unlikely to significantly change from chemical reaction with ozone. As an example, the ozonolysis of oleic acid (real component of the refractive index (RI) = 1.47), one of the tail components of the unsaturated lipid, produces products such as nonanoic acid (RI = 1.43) and azelaic acid (RI = 1.43)).[146]

A single wavelength of light of 500 nm was used in the N-Mie model to be broadly representative of shortwave wavelengths within the lower atmosphere. The optical properties of an atmospheric aerosol were simplified to the single scattering albedo, ω, and the asymmetry parameter (the average of the cosine of the scattering angle of light by the particle), g. The value of ω ranges from 0 (completely absorbed) to 1 (completely scattered), and the value of g ranges from −1 (backward scattering) to 1 (forward scattering). The complex refractive indices of the components of the aerosol model were obtained from experimentally acquired measurements at 500 nm for silica (complex refractive index, $n = 1.45 + 0.00i$),[147] atmospheric organics ($n = 1.54 + 0.01i$),[12,148] and water ($n = 1.34 + 0.00i$).[149] The imaginary components of the complex refractive indices for water and silica were considered negligible. The thickness of the organic film was varied from 0.1 to 10 nm (0.1 nm steps), and the water film from 1 to 100 nm (1 nm steps). The values of ω and g for an aerosol particle with a given organic and water film thickness on a range of mineral core sizes between 10–1000 nm (10 nm steps between 10–100, 100 nm steps between 100–1000) were calculated. The values of ω and g for a "typical" aerosol particle with a given organic and water film thickness were determined by producing a weighted average of the values of ω and g for core sizes in a range of 10 to 1000 nm. The values of ω and g for a given organic and water film thickness were weighted according to a number density distribution of the urban atmospheric aerosol size distribution given by Jaenicke,[33] where the weighting was relative to the radius of the core. A summary of the N-Mie modelling parameters used herein is presented in Table 1.

Table 1 Properties of multi-layered aerosol particles, including layer position and description, thickness range (δ), modelling step size ($\Delta\delta$), and complex refractive index (RI). The step size increases with particle size to maintain computational efficiency while resolving smaller layers accurately

Layer	Description	δ/nm	$\Delta\delta$/nm	RI
Core	Silica core	10–1000	10/100	(1.45, 0.00)
Inner shell	Organic film	0.1–10	0.1	(1.54, 0.01)
Outer shell	Water film	1–100	1	(1.34, 0.00)

To determine the effect of an organic film on the light scattering properties of an aerosol at the mineral–water (and for comparison, air–water) interface, the differences in single scattering albedo $\Delta\omega$ and asymmetry parameter Δg were computed, as described in eqn (4) and (5).

$$\Delta\omega = \omega_{\text{coated}} - \omega_{\text{uncoated}} \quad (4)$$

$$\Delta g = g_{\text{coated}} - g_{\text{uncoated}} \quad (5)$$

The total size of the coated and uncoated aerosol were kept constant for this comparison, to eliminate any size related changes to ω and g, as shown in Fig. 1.

N-Mie was tested against Bohren & Huffman[143] and MiePlot[150] to ensure the models were in agreement for single homogeneous sphere and core–shell calculations of ω and g for the size range and optical properties used in the work presented here.

2.5 Aerosol forcing efficiency

The mean of the annual, global effect of an aerosol on the top of atmosphere aerosol forcing, ΔF can be estimated using a given value for aerosol single scattering albedo, ω, backscattering efficiency, b, and optical depth (AOD), τ. In the current work, the values of aerosol single scattering albedo and backscattering efficiency can be calculated from the Mie scattering calculation,

allowing the value of aerosol radiative forcing per unit optical depth (aerosol forcing efficiency) as described elsewhere,[151,152] presented in eqn (6), to be calculated.

$$\frac{\Delta F}{\tau} = -DS_0 {T_{at}}^2 (1 - A_c)\omega\beta\left\{(1 - R_s)^2 - \left(\frac{2R_s}{\beta}\right)\left[\left(\frac{1}{\omega}\right) - 1\right]\right\} \quad (6)$$

where D is the fractional day length (0.5), S_0 is the solar constant (1370 W m^{-2}), T_{at} is the atmospheric transmittance (0.76), A_c is the fractional cloud amount (0.6), and R_s is the surface reflectance (0.15), and β is the average upscatter fraction, which can be approximated by $\beta = 0.0817 + 1.8495b - 2.9682b^2$. The values of these parameters are those recommended by Haywood and Shine.[151]

The results calculated using eqn (6) for an aerosol with and without a thin, interfacial film are used to determine the change in aerosol forcing efficiency owing to the presence of a thin film at the aerosol air–water and mineral–water interface $\left(\Delta\frac{\Delta F}{\tau}\right)$ and presented alongside the respective values of $\Delta\omega$ and Δg.

3 Results

The results presented here combine neutron reflectometry, Mie scattering, and aerosol forcing efficiency calculations. The neutron reflectometry measurements are used to determine the thickness of thin organic films at the mineral–water interface, and investigate how these films change with time (see Fig. 3). The model, N-Mie, is then used to calculate the change in single scattering albedo and asymmetry parameter owing to the presence of thin films of experimentally-measured thicknesses at the air–water *versus* mineral water interface. Mie scattering calculations are also made for films of varying thicknesses at the mineral–water interface. The results from the N-Mie model were then used to approximate the change in aerosol forcing efficiency owing to the presence of the interfacial organic film.

3.1 Initial characterisation of bilayers

Neutron reflectometry measurements confirmed the presence of a deposited film at the mineral–water interface in all samples studied, as evidenced by a noticeable change in the reflectivity profiles before and after vesicle deposition (see Fig. 3). The formation of lipid bilayers at the mineral–water interface was verified by optimizing scattering length density models based on the structure shown in Fig. 4, which reproduced the measured reflectivity data. The optimization of the scattering length density models provided values for the approximate thickness of the overall bilayer used in the Mie Modelling. Note that the surface coverage of lipid bilayers can vary between substrates.

3.2 Exposure of films to ozone

Fig. 5 shows an approximation for the relative proportion of the DPPC, POPC and DOPC bilayers remaining at the mineral–water interface as a function of the duration the films were exposed to 42 μmol per dm^3 aqueous ozone. The proportion of material in the POPC and DOPC bilayers decreased over the first ~1000 s, to approximately 40% and 10% of the original film respectively, at which point no more material was lost for the rest of the measurement period. The proportion of material in the DPPC bilayer did not appear to be altered by exposure to 42 μmol dm^{-3} ozone over ~8000 s.

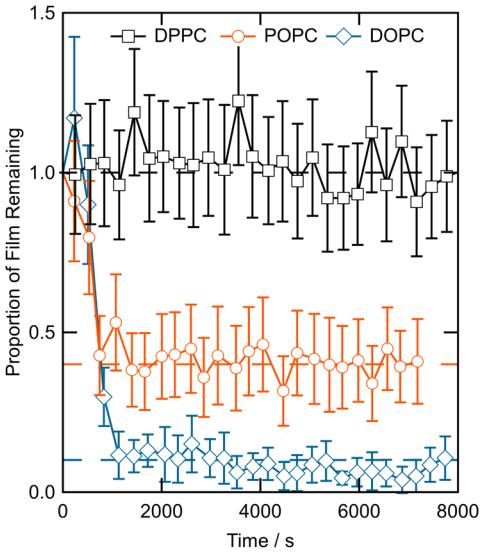

Fig. 5 The proportion of material remaining at the mineral–water interface as a function of time exposed to 42 μmol dm^{-3} ozone, determined directly from the total neutron counts.

Fig. 6 presents the scattering length density of the POPC and DOPC bilayers as a function of time and distance from the interface, when exposed to aqueous ozone of concentrations of 8.3 and 2.1 μmol dm^{-3}, respectively. As regions of the plot darken with time, this can be interpreted as organic material being replaced with water, highlighting a reduction in overall film thickness but some material remains. The decrease in ozone concentration slowed the rate of loss of material from the interface from ~1000 s in 42 μmol dm^{-3} ozone, to ~5000 s for POPC in 8.3 μmol dm^{-3}, and ~30 000 s for DOPC in 2.1 μmol dm^{-3}. The use of significantly lower concentrations of ozone allowed the acquisition of the more detailed structural information presented in Fig. 6. The method used in Fig. 6 provides unprecedented graphic detail regarding what is happening at the mineral–water interface and allows mechanistic details to be elucidated.

3.3 Light scattering and aerosol forcing efficiency

Fig. 7 shows the changes in single scattering albedo, asymmetry parameter and aerosol forcing efficiency of a model mineral aerosol owing to the presence of a 1 nm thick organic film at the mineral–water or air–water interface (as shown in Fig. 1) as a function of the thickness of the water layer, where the water layer thickness varies between 1–100 nm. For the model particle with the organic layer at the air–water interface, the value of $\Delta\omega$ varies from -3.5×10^{-3} to -0.8×10^{-3}, the values of Δg vary from 3.8×10^{-3} to 0.5×10^{-3}, and the values of $\Delta\frac{\Delta F}{\tau}$ vary from

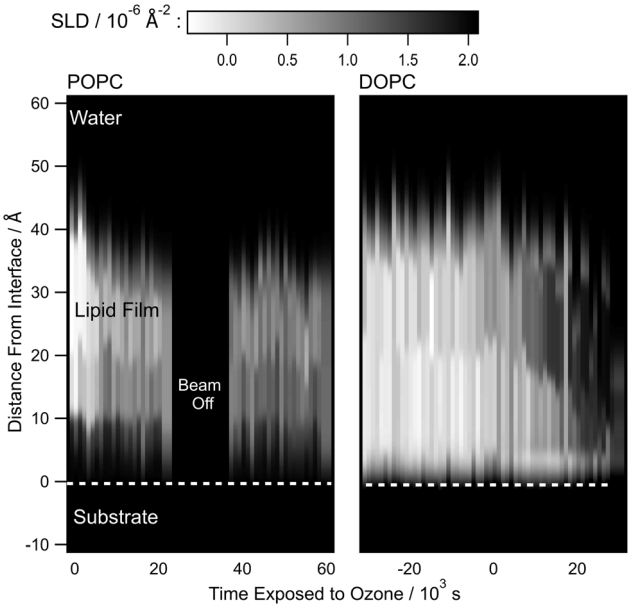

Fig. 6 The scattering length density profiles of POPC and DOPC bilayers at the mineral–water interface as a function of time when exposed to continuously flown aqueous ozone (8.3 μmol dm^{-3} for POPC, 2.1 μmol dm^{-3} for DOPC). The brightness intensity of the plot is determined by the scattering length density, allowing clear identification of different film components and changes over time. Sample components with a scattering length density equal to the scattering length density of the solution, *i.e.*, 2.065 × 10^{-6} Å^{-2}, are shown in black, while lighter shading indicates a lower scattering length density. Thus, a decrease in component brightness is considered representative of the film decaying away and being replaced with silicon contrast-matched water. Aqueous solutions of ozone are added when the exposure time is zero.

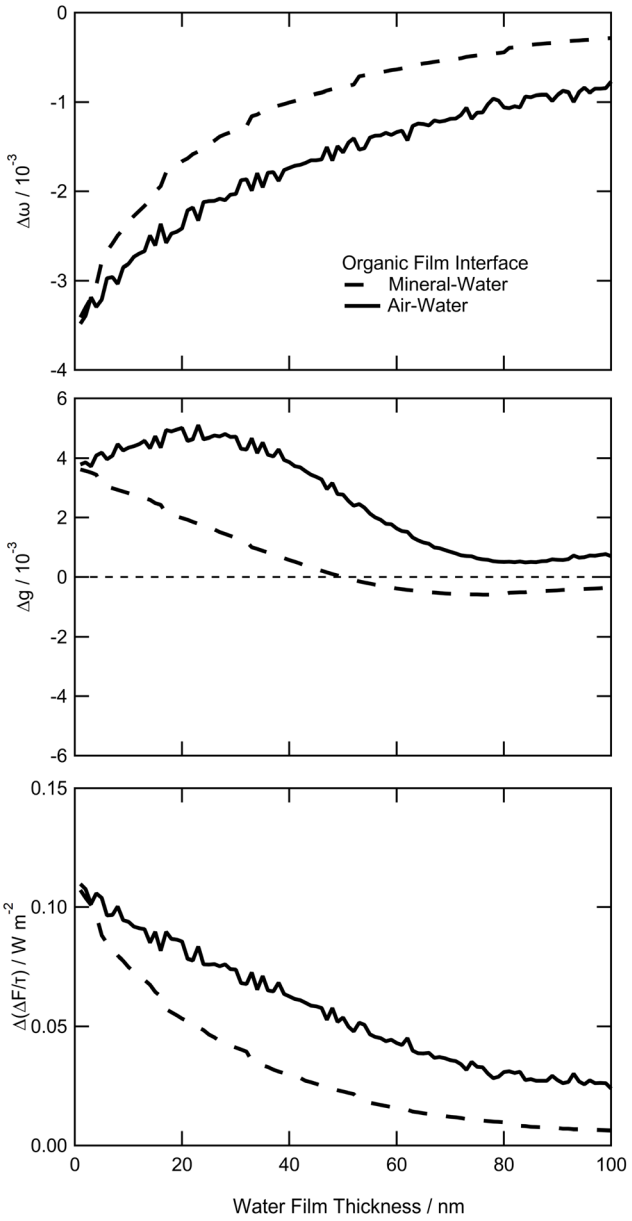

Fig. 7 Modeled changes in single scattering albedo, asymmetry parameter, and aerosol forcing efficiency for a model water-coated silica particle owing to the presence of a 1 nm thick organic film located at either the mineral–water or air–water interface. The parameters are shown as a function of water layer thickness, varying from 1 to 100 nm.

0.11 to 0.03 W m^{-2}. For the model particle with the organic film at the mineral–water interface, the value of $\Delta\omega$ vary from -3.4×10^{-3} to -0.3×10^{-3}, Δg varies from 3.6×10^{-3} to -0.6×10^{-3}, and the values of $\Delta\frac{\Delta F}{\tau}$ vary from 0.11 to 0.01 W m^{-2}.

Fig. 8 shows the values of $\Delta\omega$, Δg, and $\Delta\frac{\Delta F}{\tau}$ as a function of the organic film thickness for a model particle with an organic film present at the mineral–water interface. The thicknesses of the organic film vary between 0.1–10 nm, and the water layer's thickness is 10 nm. The results in Fig. 8 demonstrate that the value of ω of the model particle decreases and the values of g and $\frac{\Delta F}{\tau}$ increase as a function of the thickness of the organic film. The greatest effect on the model particles considered here was for an organic film at 10 nm, which produced a value of -0.016 for $\Delta\omega$, 0.025 for Δg, and 0.52 W m^{-2} for $\Delta\frac{\Delta F}{\tau}$.

The Mie scattering calculations presented here were performed for light with a wavelength of 500 nm, chosen to be broadly representative of shortwave solar radiation in the lower atmosphere. At longer wavelengths, the size parameter of a given aerosol particle decreases which tends to increase the ratio of forward scattered light, relative to backward scattered light, thus increasing the value of the asymmetry parameter, g. It could be expected that there would be a decrease light absorption by the particle with wavelength in the visible regime, increasing the value of the single scattering albedo, ω. The inverse is expected at shorter wavelengths. However, it should be noted that such suggestions are tendencies only and a Mie scattering calculation should be performed. Also given the complex interplay of scattering and absorption effects introduced by a thin interfacial film, the values of $\Delta\omega$ and Δg for an aerosol particle of a given morphology are wavelength-dependent, and accurate determination would require individual calculation at each wavelength of interest.

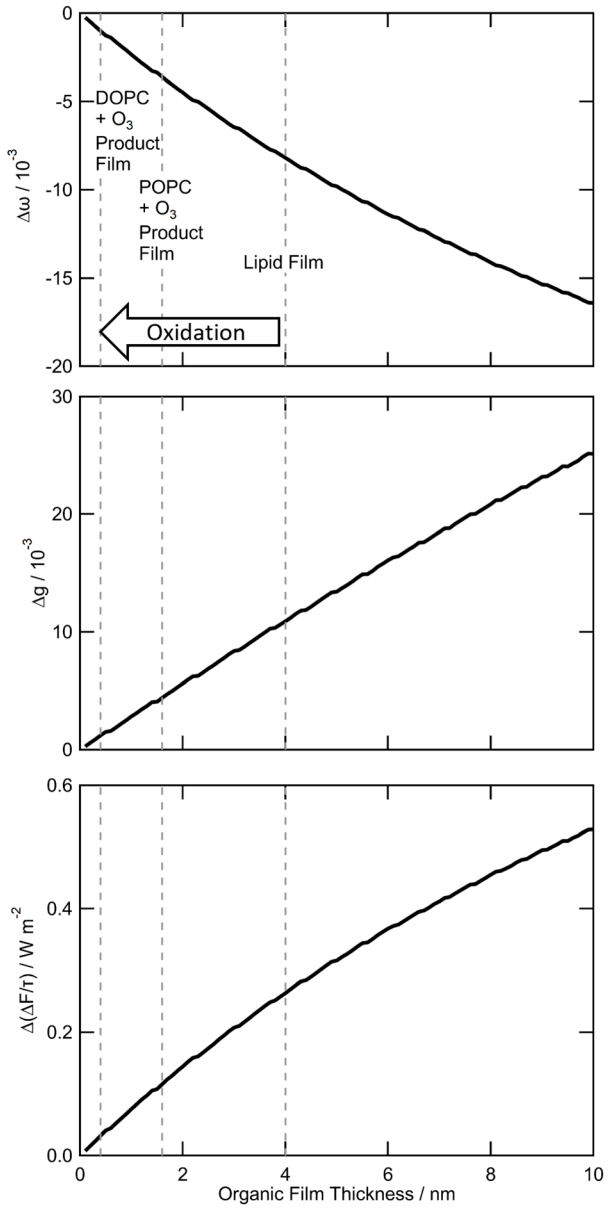

Fig. 8 The calculated change in single scattering albedo, asymmetry parameter, and aerosol forcing efficiency of a silica particulate coated in a 10 nm thick water film owing to the presence of an organic film of 0.1–10 nm thickness at the mineral–water interface. The dashed lines provide a guide to contextualise the results of the experimental component of this work.

4 Discussion

4.1 Film oxidation

The results depicted in Fig. 6 demonstrate that lipid bilayers at the mineral–water interface, containing molecules with unsaturated carbon–carbon double bonds, are susceptible to oxidation by aqueous ozone which can penetrate the bilayer. After the lipid bilayers were exposed to aqueous ozone for extended periods of time (POPC; 42 μmol dm^{-3} for 6000 s & 8.3 μmol dm^{-3} for 40 000 s, DOPC; 42 μmol dm^{-3} for 6000 s & 2.1 μmol dm^{-3} 40 000 s) a product film appeared to form that persisted at the mineral–water interface and resisted further oxidation by ozone. The proportion of the original organic film removed from the mineral–water interface due to oxidation by aqueous ozone depended on the number of unsaturated double bonds in the film, with higher ozone concentrations increasing the rate of material loss. The results presented here are consistent with the results of both experimental observations[88,153,154] and molecular dynamics simulations.[155–158] Thompson *et al.*[159] studied the oxidation of a phosphocholine lipid, POPC, at the air–water interface and noted that any reactive intermediate (by inference here a Criegee intermediate) does not react intermolecularly with another lipid molecule or intra-moleculary with the other hydrocarbon 'tail' of the lipid but that bond scission occurs with material leaving the interface. The scattering length density profiles with time in Fig. 6 support equivalent chemistry occurring at the silica–water interface as shown in the simplified and stylised chemical mechanisms in Fig. 9 and 10.

4.2 Light scattering and aerosol forcing efficiency

The experimental component of this work measured the thicknesses of lipid bilayers at the mineral–water interface, the values of which were used to approximate the thickness of lipid-like films at the same interface on atmospheric aerosol particulates. The lipid films measured before and after oxidation (approximately 4 nm, 1.6 nm, and 0.4 nm based on the proportion of material remaining after oxidation shown in Fig. 5), and thus the light-scattering modelling and aerosol-forcing efficiency calculations based on these values, represent interfacial films that are considerably thinner than those investigated in many core–shell studies such as Hu *et al.* (2021)[160] (core is ∼12% of the total particle mass), Hu *et al.* (2023)[161] (∼2%) and Hartikainen *et al.* (2025)[162] (0.02–10%). Comparisons between the results presented here and studies of core–shell aerosols with substantially thicker films should be made with caution, as differences in organic film or shell thickness may limit the direct comparability of these works.

The light scattering effects of thin films on atmospheric aerosol have previously been modelled using experimental measurements performed by the authors of this work, including using complex refractive indexes determined from laser trapping experiments[12,148] and film thicknesses obtained through X-ray and neutron reflectometry.[10,11] These works[10–12,148] conclude that thin, interfacial films at the air–water, and mineral–air, interface have atmospherically significant effects on the light scattering of atmospheric aerosol particles. The results presented here in Fig. 7 demonstrate that organic films of 1 nm thickness broadly have a similar order of magnitude effect on the light scattering of an aerosol particle regardless of whether the film is located at the air–water or mineral–water interface, over a range of water layer thicknesses of 1–100 nm. Interestingly, as the thickness of the water layer increases, both $\Delta\omega$ and $\Delta\frac{\Delta F}{\tau}$ follow very similar trends between the model with the organic film at the air–water, and mineral–water interface. However, there is some variation in the changes to Δg as a function of water layer thickness.

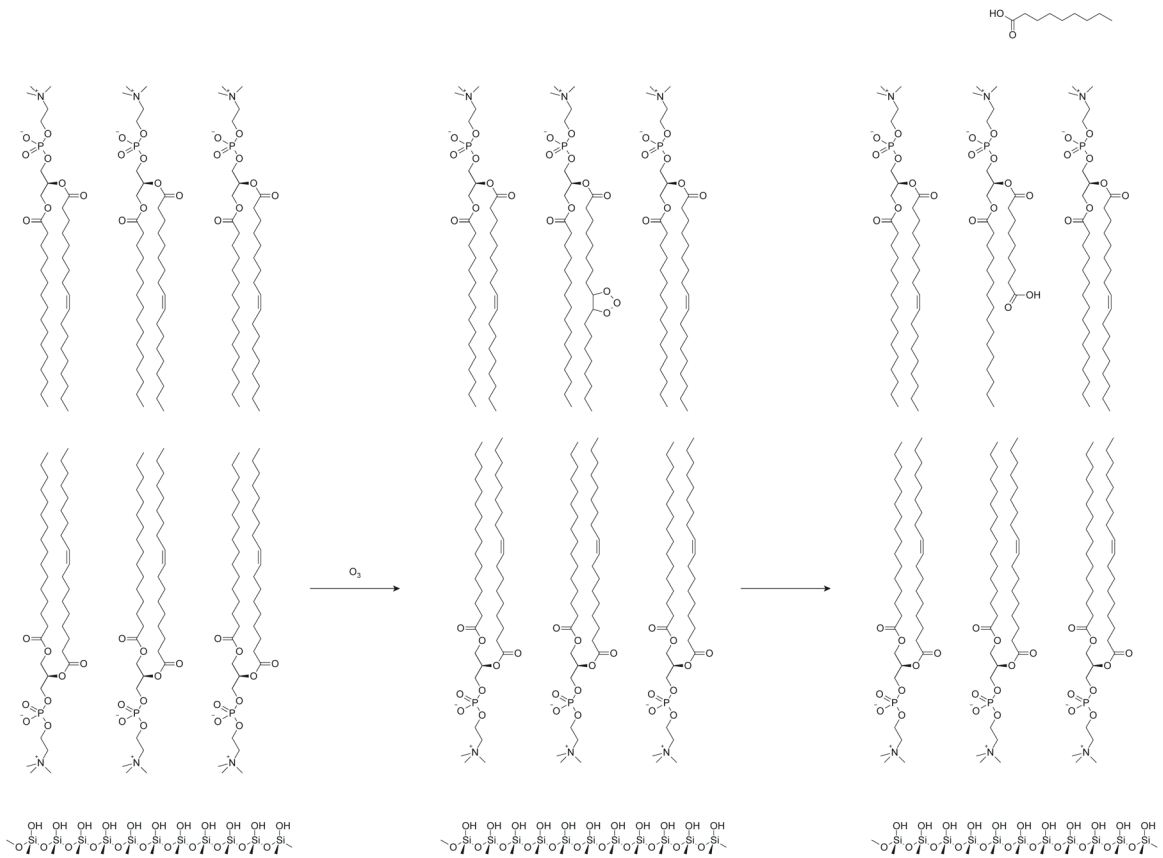

Fig. 9 A 'cartoon' chemical mechanism for the initial reaction of aqueous ozone with a bilayer of POPC at the air–water interface, demonstrating the ozonolysis and bond scission of the carbon–carbon double bond to produce two carboxylic acid groups and the loss of nonanoic acid to the bulk solution based on the chemistry reported in Thompson *et al.*[159] Note the ozonolysis of the double bond is shown producing carboxylic acid groups but may produce aldehydes, alcohol or peroxy hydroxy groups. The diagram is for the initial reaction and the remaining double bonds in the film will react removing some material from the interface but leaving a slightly thinner film with less material at the interface as consistent with Fig. 6.

Broadly, Fig. 8 demonstrates that for a model aerosol particle with an organic film at the mineral–water interface, both the light absorbed and the light forward scattered increase as a function of the organic film thickness. When considering the experimental observations of the current work with the results of the modelling shown in Fig. 8 (where the dashed lines

Fig. 10 A 'cartoon' chemical mechanism for the initial reaction of aqueous ozone with a bilayer of DOPC at the air–water interface, demonstrating the ozonolysis and bond scission of the carbon–carbon double bond to produce two carboxylic acid groups and the loss of two nonanoic acids and remnants of the DOPC lipid to the bulk solution based on the chemistry reported in Thompson *et al.*[159] The diagram is for the initial reaction and the remaining double bonds in the film will react removing the majority of the lipid material from the interface as consistent with Fig. 6.

indicate the thicknesses of pristine and oxidised films), it is evident that the oxidation of lipid-like films containing unsaturated carbon–carbon double bonds at the mineral–water interface would decrease, but not entirely remove, the influence of the organic film on the optical properties of the aerosol particle. For example, the results depicted in Fig. 8 indicate that oxidation of a pristine lipid-like film (approximately 4 nm) by aqueous ozone (to approximately 0.4 nm) would change the values of $\Delta\omega$, Δg, and $\Delta\frac{\Delta F}{\tau}$ from −0.08, 0.011, and 0.26 W m^{-2} to −0.001, 0.001 and 0.03 W m^{-2}, respectively.

A similar approach to the current work was taken in Shepherd *et al.*[11] where the authors estimated the changes to ω and g owing to the oxidation of an organic film at the atmospheric aerosol air–water and mineral–air interface by gas-phase hydroxyl radicals, and this oxidation is approximated to be a halving of the film thickness. Note, that Shepherd *et al.* uses a core–shell (two-layer) system of a mineral core and organic shell, or water core and organic shell. Similarly to the current work, Shepherd *et al.* suggest that the oxidation of thin films at the air–water and solid–air interface of "urban" aerosol would result in an increase in the ω of the aerosol particulate and a decrease in g. The results in Fig. 9 of Shepherd *et al.* indicate the oxidation of a 4 nm thick organic thin film will cause an increase in ω of approximately 0.02 and a decrease in g of 0.01. Comparatively, in the work presented here, the oxidation of an organic film of 4 nm thickness is found to cause an increase of 0.004 in ω and a decrease of 0.004 in g. Comparison with Shepherd *et al.* shows that oxidation of thin organic films induces similar-magnitude changes in aerosol ω and g, regardless of the film's interface.

The results of the work presented here and in Shepherd *et al.* are applicable to particulates with highly scattering, weakly absorbing cores, however the effect of organic thin films may have different behaviours on more absorbing cores such as black carbon. Hu *et al.*[161] demonstrate experimentally that the development of organic films, with similar absorption to those used here, on the surface of black carbon cores results in an increase in the aerosol's ω as the film thickness increases. While Hu *et al.* use significantly larger shell to core ratios than here, a comparison of their work and the work presented here demonstrates the variable effects that organic thin films may have on different host particulates.

5 Atmospheric implications

It is demonstrated here that the presence of an organic film at the presence of an organic film at the mineral–water interface of an atmospheric aerosol particle has significant effects on the optical properties of the aerosol, and these effects are of a similar order of magnitude regardless of the interface the film is present at. As shown in Fig. 7, when the thickness of the water component of a model aerosol particle changes, such as during cloud processing, the ω and $\frac{\Delta F}{\tau}$ of each aerosol particle model varies similarly regardless of the interface the organic film is present at, while changes in g are different. The differences in Δg highlight an interface-specific effect that organic thin films may have on aerosol optical properties, suggesting that films of the same thickness can influence the atmospheric impact of aerosols in similar yet distinct ways depending on the interface it is present at. Furthermore, the similarities in magnitude of the values of Δg and $\Delta\omega$ in this study and those from Shepherd *et al.*[11] indicate that, similarly to Shepherd's conclusions for thin films at the air–water interface, organic films at the mineral–water interface may also affect the top-of-atmosphere albedo.

The effect of an organic film at the mineral–water interface has been shown to increase in magnitude as a function of the organic film thickness, depicted in Fig. 8. The increase in $\frac{\Delta F}{\tau}$ as a function of organic film thickness shown in Fig. 8 effectively demonstrates the warming effect on the atmosphere of organic films at the mineral–water interface of atmospheric particles. The experimental component of this work has demonstrated that the oxidation of films containing proxies for atmospheric organic material would reduce the thickness of these films, ultimately having a small cooling effect. The experimental component of the work presented here also validates the findings of the Mie modelling by demonstrating that atmospherically relevant organic materials can adsorb to the mineral–water interface, replicating one formation pathway of organic thin films at the atmospheric aerosol mineral–water interface. Atmospherically relevant proxy organic films have been shown to remain at the interface despite a continuous flow of water, suggesting that films of similar thickness and material may remain stable at the aerosol mineral–water interface in atmospheric contexts, unless disrupted by photochemical reaction.

The work presented here also shows that organic films containing unsaturated carbon–carbon double bonds are partially removed from the mineral–water interface through oxidation by aqueous ozone. The removal of organic films from the mineral–water interface reduces the film thickness in a manner that may influence aerosol optical properties. However, despite oxidation, some organic material remains at the interface regardless of the number of carbon–carbon double bonds in the organic material. The persistence of some material at the mineral–water interface suggests that aqueous ozone may not be sufficient for the complete removal of organic films, allowing these films, and their impacts on ω g, and $\frac{\Delta F}{\tau}$ to persist throughout an aerosol's atmospheric lifetime, depending on the action of other atmospherically relevant oxidants.

6 Conclusions

Three lipids with varying numbers of carbon–carbon double bonds, DPPC, POPC, and DOPC, were deposited at the silica–water interface of a silicon block and all appeared to form films of approximately 4 nm in thickness.

Exposure of the POPC and DOPC films to aqueous ozone resulted in the films decaying to approximately 40% and 10% of their respective pristine films, where the product films appeared

to resist further oxidation by ozone. The DPPC film did not appear to change under exposure to aqueous ozone.

The results of the Mie modelling and aerosol forcing efficiency approximation indicated that a film thickness of up to 10 nm could decrease the aerosol particle's single-scattering albedo (ω) by 0.016, increase the asymmetry parameter (g) by 0.025, and increase the aerosol forcing efficiency $\left(\frac{\Delta F}{\tau}\right)$ by 0.52 W m^{-2}. It was also shown that organic films of the same thickness have a similar order of magnitude of effects on the light scattering of aerosol particle regardless of whether the film is at the air–water or mineral–water interface. Consideration of the thickness measurements taken using neutron reflectometry demonstrated that the oxidation of organic films at the mineral–water interface of an atmospheric aerosol can significantly alter the optical effects the film has on the aerosol.

The results presented here demonstrate the ability for atmospherically relevant organic material to adsorb at the mineral–water interface, forming thin films that can have important optical effects on their host aerosol. Thin films at the mineral–water interface have been shown to be susceptible to oxidation by ozone, relative to the number of carbon–carbon double bonds present within the material, and it has been shown that this oxidation can result in significant changes to the optical effects of the thin film which may be interpreted as a minor cooling effect. Owing to the results presented here, it is evident that organic thin films at the aerosol mineral–water interface should be considered for implementation into larger scale aerosol chemistry models in order to further determine the significance of these thin films in the atmosphere.

Author contributions

Contributions have been defined by the CRediT contributor role taxonomy. Edward J. Stuckey: data curation, formal analysis, investigation, methodology, software, validation, visualization, writing – original draft, writing – review & editing. Rebecca J. L. Welbourn: data curation, formal analysis, funding acquisition, investigation, methodology, project administration, resources, software, supervision, validation, writing – review & editing. Tobias W. D. Robson: formal analysis, investigation, writing – review & editing. Philipp Gutfreund: investigation, resources, writing – review & editing. Katherine C. Thompson: investigation, writing – review & editing. Adrian R. Rennie: investigation, writing – review & editing. Martin D. King: conceptualization, funding acquisition, investigation, methodology, project administration, resources, supervision, validation, writing – review & editing.

Conflicts of interest

There are no conflicts to declare.

Data availability

The data presented in this article are available as part of the ISIS & ILL open access data policy. See DOI: https://doi.org/10.5286/ISIS.E.RB1820245, https://doi.org/10.5286/ISIS.E.RB2210207-1, https://doi.org/10.5286/ISIS.E.RB2210371-2, https://doi.org/10.5286/ISIS.E.RB2210371-1, https://doi.org/10.5291/ILL-DATA.9-10-1517 and https://doi.org/10.5291/ILL-DATA.9-10-1241. Data for experiment 9-10-1079 is available through the ILL legacy data portal for measurement numbers 082149–082474.

Acknowledgements

The authors would like to acknowledge the work by the support network at the ISIS Neutron and Muon Source and the Institut Laue-Langevin for providing the beam time and making this experiment possible by maintaining the facility, providing engineering help for our sample environment and providing constant support throughout the experiments RB1820245, RB2210207, RB2210371(ISIS), and 9-10-1079, 9-10-1517, and 9-10-1241(ILL). Acknowledgements are made to NERC (NE/T00732X/1) for funding this work.

References

1 P. S. Gill, T. E. Graedel and C. J. Weschler, *Rev. Geophys.*, 1983, **21**, 903.
2 D. J. Donaldson and V. Vaida, *Chem. Rev.*, 2006, **106**, 1445–1461.
3 J. F. Davies, R. E. Miles, A. E. Haddrell and J. P. Reid, *Proc. Natl. Acad. Sci. U. S. A.*, 2013, **110**, 8807–8812.
4 D. B. Collins and V. H. Grassian, in *Gas-liquid Interfaces in the Atmosphere: Impacts, Complexity, and Challenges*, Elsevier, 2018, pp. 271–313.
5 G. B. Ellison, A. F. Tuck and V. Vaida, *J. Geophys. Res. Atmos.*, 1999, **104**, 11633–11641.
6 H. Tervahattu, J. Juhanoja, V. Vaida, A. F. Tuck, J. Niemi, K. Kupiainen, M. Kulmala and H. Vehkamäki, *J. Geophys. Res. Atmos.*, 2005, **110**, D06207.
7 D. A. Lack and C. D. Cappa, *Atmos. Chem. Phys.*, 2010, **10**, 4207–4220.
8 C. H. Song and G. R. Carmichael, *Atmos. Environ.*, 1999, **33**, 2203–2218.
9 T. Eliason, J. Gilman and V. Vaida, *Atmos. Environ.*, 2004, **38**, 1367–1378.
10 R. H. Shepherd, M. D. King, A. R. Rennie, A. D. Ward, M. M. Frey, N. Brough, J. Eveson, S. D. Vento, A. Milsom, C. Pfrang, M. W. A. Skoda and R. J. L. Welbourn, *Environ. Sci.: Atmos.*, 2022, **2**, 574–590.
11 R. H. Shepherd, M. D. King, A. D. Ward, E. J. Stuckey, R. J. L. Welbourn, N. Brough, A. Milsom, C. Pfrang and T. Arnold, *Atmos. Chem. Phys.*, 2025, **25**, 2569–2588.
12 C. R. Barker, M. L. Poole, M. Wilkinson, J. Morison, A. Wilson, G. Little, E. J. Stuckey, R. J. L. Welbourn, A. D. Ward and M. D. King, *Environ. Sci.: Atmos.*, 2023, **3**, 1008–1024.
13 C. S. Zender, R. L. L. Miller and I. Tegen, *EOS Trans. Am. Geophys. Union*, 2004, **85**, 509–512.
14 P. R. Buseck and M. Pósfai, *Proc. Natl. Acad. Sci. U. S. A.*, 1999, **96**, 3372–3379.

15 M. O. Andreae, R. J. Charlson, F. Bruynseels, H. Storms, R. V. Grieken and W. Maenhaut, *Science*, 1986, **232**, 1620–1623.
16 C. Textor, M. Schulz, S. Guibert, S. Kinne, Y. Balkanski, S. Bauer, T. Berntsen, T. Berglen, O. Boucher, M. Chin, F. Dentener, T. Diehl, R. Easter, H. Feichter, D. Fillmore, S. Ghan, P. Ginoux, S. Gong, A. Grini, J. Hendricks, L. Horowitz, P. Huang, I. Isaksen, I. Iversen, S. Kloster, D. Koch, A. Kirkevåg, J. E. Kristjansson, M. Krol, A. Lauer, J. F. Lamarque, X. Liu, V. Montanaro, G. Myhre, J. Penner, G. Pitari, S. Reddy, O. Seland, P. Stier, T. Takemura and X. Tie, *Atmos. Chem. Phys.*, 2006, **6**, 1777–1813.
17 R. A. McCormick and J. H. Ludwig, *Science*, 1967, **156**, 1358–1359.
18 R. W. Bergstrom, P. Pilewskie, P. B. Russell, J. Redemann, T. C. Bond, P. K. Quinn and B. Sierau, *Atmos. Chem. Phys.*, 2007, **7**, 5937–5943.
19 J. Li, B. E. Carlson, Y. L. Yung, D. Lv, J. Hansen, J. E. Penner, H. Liao, V. Ramaswamy, R. A. Kahn, P. Zhang, O. Dubovik, A. Ding, A. A. Lacis, L. Zhang and Y. Dong, *Nat. Rev. Earth Environ.*, 2022, **3**, 363–379.
20 J. F. Kok, T. Storelvmo, V. A. Karydis, A. A. Adebiyi, N. M. Mahowald, A. T. Evan, C. He and D. M. Leung, *Nat. Rev. Earth Environ.*, 2023, **4**, 71–86.
21 V. A. Karydis, P. Kumar, D. Barahona, I. N. Sokolik and A. Nenes, *J. Geophys. Res. Atmos.*, 2011, **116**, D23204.
22 P. Kumar, I. N. Sokolik and A. Nenes, *Atmos. Chem. Phys.*, 2011, **11**, 3527–3541.
23 H. Herich, T. Tritscher, A. Wiacek, M. Gysel, E. Weingartner, U. Lohmann, U. Baltensperger and D. J. Cziczo, *Phys. Chem. Chem. Phys.*, 2009, **11**, 7804.
24 S. E. Bauer, Y. Balkanski, M. Schulz, D. A. Hauglustaine and F. Dentener, *J. Geophys. Res. Atmos.*, 2004, **109**, D02304.
25 F. J. Dentener, G. R. Carmichael, Y. Zhang, J. Lelieveld and P. Crutzen, *J. Geophys. Res. Atmos.*, 1996, **101**(22), 869–889.
26 V. H. Grassian, *J. Phys. Chem. A*, 2002, **106**, 860–877.
27 C. R. Usher, A. E. Michel and V. H. Grassian, *Chem. Rev.*, 2003, **103**, 4883–4940.
28 T. Claquin, M. Schulz, Y. Balkanski and O. Boucher, *Tellus B*, 1998, **50**, 491.
29 L. Su and O. B. Toon, *Atmos. Chem. Phys.*, 2011, **11**, 3263–3280.
30 M. Masmoudi, M. Chaabane, D. Tanré, P. Gouloup, L. Blarel and F. Elleuch, *Atmos. Res.*, 2003, **66**, 1–19.
31 N. Mahowald, C. Luo, J. Corral and C. Zender, *J. Geophys. Res. Atmos.*, 2003, **108**, 4206.
32 O. Dubovik, B. Holben, T. F. Eck, A. Smirnov, Y. J. Kaufman, M. D. King, D. Tanré and I. Slutsker, *J. Atmos. Sci.*, 2002, **59**, 590–608.
33 R. Jaenicke, *Science*, 2005, **308**, 73.
34 C. Denjean, F. Cassola, A. Mazzino, S. Triquet, S. Chevaillier, N. Grand, T. Bourrianne, G. Momboisse, K. Sellegri, A. Schwarzenbock, E. Freney, M. Mallet and P. Formenti, *Atmos. Chem. Phys.*, 2016, **16**, 1081–1104.
35 E. R. Gibson, *Geophys. Res. Lett.*, 2006, **33**, L13811.
36 C. L. Ryder, E. J. Highwood, A. Walser, P. Seibert, A. Philipp and B. Weinzierl, *Atmos. Chem. Phys.*, 2019, **19**, 15353–15376.
37 M. Tang, X. Huang, K. Lu, M. Ge, Y. Li, P. Cheng, T. Zhu, A. Ding, Y. Zhang, S. Gligorovski, W. Song, X. Ding, X. Bi and X. Wang, *Atmos. Chem. Phys.*, 2017, **17**, 11727–11777.
38 P. K. Mogili, K. H. Yang, M. A. Young, P. D. Kleiber and V. H. Grassian, *J. Geophys. Res. Atmos.*, 2007, **112**(D21204).
39 S. E. Bauer, M. I. Mishchenko, A. A. Lacis, S. Zhang, J. Perlwitz and S. M. Metzger, *J. Geophys. Res. Atmos.*, 2007, **112**, D06307.
40 O. Möhler, S. Benz, H. Saathoff, M. Schnaiter, R. Wagner, J. Schneider, S. Walter, V. Ebert and S. Wagner, *Environ. Res. Lett.*, 2008, **3**, 025007.
41 M. Brüggemann, N. Hayeck, C. Bonnineau, S. Pesce, P. A. Alpert, S. Perrier, C. Zuth, T. Hoffmann, J. Chen and C. George, *Faraday Discuss.*, 2017, **200**, 59–74.
42 S. H. Jones, M. D. King, A. R. Rennie, A. D. Ward, R. A. Campbell and A. V. Hughes, *J. Phys. Chem. A*, 2023, **127**, 8922–8934.
43 K. S. Docherty and P. J. Ziemann, *J. Phys. Chem. A*, 2006, **110**, 3567–3577.
44 I. J. George, A. Vlasenko, J. G. Slowik, K. Broekhuizen and J. P. D. Abbatt, *Atmos. Chem. Phys.*, 2007, **7**, 4187–4201.
45 A. T. Lambe, A. T. Ahern, L. R. Williams, J. G. Slowik, J. P. S. Wong, J. P. D. Abbatt, W. H. Brune, N. L. Ng, J. P. Wright, D. R. Croasdale, D. R. Worsnop, P. Davidovits and T. B. Onasch, *Atmos. Meas. Tech.*, 2011, **4**, 445–461.
46 C. Y. Lim, E. C. Browne, R. A. Sugrue and J. H. Kroll, *Geophys. Res. Lett.*, 2017, **44**, 2949–2957.
47 A. T. Lambe, C. D. Cappa, P. Massoli, T. B. Onasch, S. D. Forestieri, A. T. Martin, M. J. Cummings, D. R. Croasdale, W. H. Brune, D. R. Worsnop and P. Davidovits, *Environ. Sci. Technol.*, 2013, **47**, 6349–6357.
48 M. D. King, A. R. Rennie, K. C. Thompson, F. N. Fisher, C. C. Dong, R. K. Thomas, C. Pfrang and A. V. Hughes, *Phys. Chem. Chem. Phys.*, 2009, **11**, 7699–7707.
49 S. E. Paulson and J. J. Orlando, *Geophys. Res. Lett.*, 1996, **23**, 3727–3730.
50 A. R. Rickard, D. Johnson, C. D. McGill and G. Marston, *J. Phys. Chem. A*, 1999, **103**, 7656–7664.
51 R. E. Keay and G. A. Hamilton, *J. Am. Chem. Soc.*, 1976, **98**, 6578–6582.
52 P. S. Bailey, *Chem. Rev.*, 1958, **58**, 925–1010.
53 W. B. Demore, *Int. J. Chem. Kinet.*, 1971, **3**, 161–173.
54 S. N. Chu, S. Sands, M. R. Tomasik, P. S. Lee and V. F. McNeill, *J. Am. Chem. Soc.*, 2010, **132**, 15968–15975.
55 Y. Pi, J. Schumacher and M. Jekel, *Water Res.*, 2005, **39**, 83–88.
56 R. R. Dickerson, D. H. Stedman and A. C. Delany, *J. Geophys. Res., Oceans*, 1982, **87**, 4933–4946.
57 E. Berezina, K. Moiseenko, A. Skorokhod, N. V. Pankratova, I. Belikov, V. Belousov and N. F. Elansky, *Atmosphere*, 2020, **11**, 1262.
58 J. A. Roth and D. E. Sullivan, *Ind. Eng. Chem. Fundam.*, 1981, **20**, 137–140.

59 J. Sotelo, F. Beltrán, F. Benitez and J. Beltrán-Heredia, *Water Res.*, 1989, **23**, 1239–1246.
60 C. G. Hewes and R. R. Davison, *AIChE J.*, 1971, **17**, 141–147.
61 M. S. Siddiqui, G. L. Amy and B. D. Murphy, *Water Res.*, 1997, **31**, 3098–3106.
62 R. E. Brandt, J. J. Schwab, P. W. Casson, U. K. Roychowdhury, D. Wolfe, K. L. Demerjian, K. L. Civerolo, O. V. Rattigan and H. D. Felton, *Aerosol Air Qual. Res.*, 2016, **16**, 873–884.
63 B. Ervens, C. George, J. E. Williams, G. V. Buxton, G. A. Salmon, M. Bydder, F. Wilkinson, F. Dentener, P. Mirabel, R. Wolke and H. Herrmann, *J. Geophys. Res. Atmos.*, 2003, **108**, 4426.
64 V. P. Aneja, C. S. Claiborn, Z. Li and A. Murthy, *Atmos. Environ.*, 1994, **28**, 1781–1790.
65 X. Zhang, K. M. Barraza and J. L. Beauchamp, *Proc. Natl. Acad. Sci. U. S. A.*, 2018, **115**, 3255–3260.
66 R. M. Kirpes, D. Bonanno, N. W. May, M. Fraund, A. J. Barget, R. C. Moffet, A. P. Ault and K. A. Pratt, *ACS Cent. Sci.*, 2019, **5**, 1760–1767.
67 J. V. Trueblood, M. R. Alves, D. Power, M. V. Santander, R. E. Cochran, K. A. Prather and V. H. Grassian, *ACS Earth Space Chem.*, 2019, **3**, 1614–1623.
68 J. A. Faust and J. P. D. Abbatt, *J. Phys. Chem. A*, 2019, **123**, 2114–2124.
69 H. Yu, W. Li, Y. Zhang, P. Tunved, M. Dall'Osto, X. Shen, J. Sun, X. Zhang, J. Zhang and Z. Shi, *Atmos. Chem. Phys.*, 2019, **19**, 10433–10446.
70 M. Passananti, L. Kong, J. Shang, Y. Dupart, S. Perrier, J. Chen, D. J. Donaldson and C. George, *Angew. Chem., Int. Ed.*, 2016, **55**, 10336–10339.
71 T. C. Burdette and A. A. Frossard, *J. Environ. Sci.*, 2021, **108**, 164–174.
72 N. Hayeck, I. Mussa, S. Perrier and C. George, *ACS Earth Space Chem.*, 2020, **4**, 1247–1253.
73 J. Shang, M. Passananti, Y. Dupart, R. Ciuraru, L. Tinel, S. Rossignol, S. Perrier, T. Zhu and C. George, *Environ. Sci. Technol. Lett.*, 2016, **3**, 67–72.
74 M. Xu, N. T. Tsona, S. Cheng, J. Li and L. Du, *Sci. Total Environ.*, 2021, **782**, 146893.
75 Y. Dubowski, J. Vieceli, D. J. Tobias, A. Gomez, A. Lin, S. A. Nizkorodov, T. M. McIntire and B. J. Finlayson-Pitts, *J. Phys. Chem. A*, 2004, **108**, 10473–10485.
76 H. C. Allen, J. M. Laux, R. Vogt, B. J. Finlayson-Pitts and J. C. Hemminger, *J. Phys. Chem.*, 1996, **100**, 6371–6375.
77 A. A. Frossard, S. M. Burrows, S. M. Elliott, T. S. Bates and P. K. Quinn, *J. Geophys. Res. Atmos.*, 2014, **119**(13), 134–146.
78 M. S. Rana and M. I. Guzman, *J. Phys. Chem. A*, 2022, **126**, 6502–6516.
79 B. M. Connelly and M. A. Tolbert, *Environ. Sci. Technol.*, 2010, **44**, 4603–4608.
80 S. Langenberg, V. Proksch and U. Schurath, *Atmos. Environ.*, 1998, **32**, 3129–3137.
81 B. A. Wellen, E. A. Lach and H. C. Allen, *Phys. Chem. Chem. Phys.*, 2017, **19**, 26551–26558.
82 J. R. Lawrence, S. V. Glass and G. M. Nathanson, *J. Phys. Chem. A*, 2005, **109**, 7449–7457.
83 S. Decesari, M. C. Facchini, S. Fuzzi and E. Tagliavini, *J. Geophys. Res. Atmos.*, 2003, **108**, 4685.
84 M. D. King, A. R. Rennie, C. Pfrang, A. V. Hughes and K. C. Thompson, *Atmos. Environ.*, 2010, **44**, 1822–1825.
85 M. D. King, S. H. Jones, C. O. Lucas, K. C. Thompson, A. R. Rennie, A. D. Ward, A. A. Marks, F. N. Fisher, C. Pfrang, A. V. Hughes and R. A. Campbell, *Phys. Chem. Chem. Phys.*, 2020, **22**, 28032–28044.
86 S. H. Jones, M. D. King, A. D. Ward, A. R. Rennie, A. C. Jones and T. Arnold, *Atmos. Environ.*, 2017, **161**, 274–287.
87 A. Milsom, A. M. Squires, I. Quant, N. J. Terrill, S. Huband, B. Woden, E. R. Cabrera-Martinez and C. Pfrang, *J. Phys. Chem. A*, 2022, **126**, 7331–7341.
88 K. C. Thompson, A. R. Rennie, M. D. King, S. J. O. Hardman, C. O. M. Lucas, C. Pfrang, B. R. Hughes and A. V. Hughes, *Langmuir*, 2010, **26**, 17295–17303.
89 C. Pfrang, K. Rastogi, E. R. Cabrera-Martinez, A. M. Seddon, C. Dicko, A. Labrador, T. S. Plivelic, N. Cowieson and A. M. Squires, *Nat. Commun.*, 2017, **8**, 1724.
90 B. Woden, M. W. A. Skoda, A. Milsom, C. Gubb, A. Maestro, J. Tellam and C. Pfrang, *Atmos. Chem. Phys.*, 2021, **21**, 1325–1340.
91 E. J. Stuckey, R. J. L. Welbourn, S. H. Jones, A. J. Armstrong, M. Wilkinson, J. I. L. Morison and M. D. King, *Environ. Sci.: Atmos.*, 2024, **4**, 1309–1321.
92 E. J. Stuckey, R. J. L. Welbourn, T. W. D. Robson, C. R. Barker, M. Wilkinson, J. I. L. Morison and M. D. King, *Atmos. Environ.*, 2026, **365**, 121690.
93 P.-M. Wu and K. Okada, *Atmos. Environ.*, 1994, **28**, 2053–2060.
94 T. M. McIntire, A. S. Lea, D. J. Gaspar, N. Jaitly, Y. Dubowski, Q. Li and B. J. Finlayson-Pitts, *Phys. Chem. Chem. Phys.*, 2005, **7**, 3605.
95 S. Sobanska, J. Barbillat, M. Moreau, N. Nuns, I. D. Waele, D. Petitprez, Y. Tobon and C. Brémard, *Phys. Chem. Chem. Phys.*, 2015, **17**, 10963–10977.
96 F. Sebastiani, R. A. Campbell, K. Rastogi and C. Pfrang, *Atmos. Chem. Phys.*, 2018, **18**, 3249–3268.
97 D. J. Donaldson and K. T. Valsaraj, *Environ. Sci. Technol.*, 2010, **44**, 865–873.
98 J. M. Anglada, M. T. Martins-Costa, J. S. Francisco and M. F. Ruiz-López, *J. Am. Chem. Soc.*, 2020, **142**, 16140–16155.
99 L. F. Voss, M. F. Bazerbashi, C. P. Beekman, C. M. Hadad and H. C. Allen, *J. Geophys. Res. Atmos.*, 2007, **112**, D06209.
100 M. Shiraiwa, C. Pfrang and U. Pöschl, *Atmos. Chem. Phys.*, 2010, **10**, 3673–3691.
101 C. Pfrang, M. Shiraiwa and U. Pöschl, *Atmos. Chem. Phys.*, 2010, **10**, 4537–4557.
102 F. Sebastiani, R. A. Campbell and C. Pfrang, *Environ. Sci.: Atmos.*, 2022, **2**, 1324–1337.
103 J. He, H. Zhang, W. Wang, Y. Ma, M. Yang, Y. He, Z. Liu, K. Yu and J. Jiang, *Environ. Res.*, 2022, **212**, 113232.
104 J. B. Gilman, H. Tervahattu and V. Vaida, *Atmos. Environ.*, 2006, **40**, 6606–6614.
105 R. Welbourn and S. Clarke, *Curr. Opin. Colloid Interface Sci.*, 2019, **42**, 87–98.

106 A. R. Rennie, M. S. Hellsing, E. Lindholm and A. Olsson, *Rev. Sci. Instrum.*, 2015, **86**, 016115.
107 J. Penfold and R. K. Thomas, *Curr. Opin. Colloid Interface Sci.*, 2014, **19**, 198–206.
108 G. Fragneto-Cusani, *J. Phys.: Condens. Matter*, 2001, **13**, 4973–4989.
109 R. P. Richter, R. Bérat and A. R. Brisson, *Langmuir*, 2006, **22**, 3497–3505.
110 A. Virkkula, H. Grythe, J. Backman, T. Petäjä, M. Busetto, C. Lanconelli, A. Lupi, S. Becagli, R. Traversi, M. Severi, V. Vitale, P. Sheridan and E. Andrews, *Atmos. Chem. Phys.*, 2022, **22**, 5033–5069.
111 D. W. Griffin, N. Kubilay, M. Koçak, M. A. Gray, T. C. Borden and E. A. Shinn, *Atmos. Environ.*, 2007, **41**, 4050–4062.
112 K. Hayakawa, N. Handa, K. Kawanobe and C. S. Wong, *Mar. Chem.*, 1996, **52**, 233–244.
113 Z. Liu, E. Van Acker, M. De Rijcke, F. Van Nieuwerburgh, C. Janssen and J. Asselman, *Environ. Int.*, 2025, **195**, 109255.
114 E. Van Acker, M. De Rijcke, Z. Liu, J. Asselman, K. A. C. De Schamphelaere, L. Vanhaecke and C. R. Janssen, *Environ. Sci. Technol.*, 2021, **55**, 15989–16000.
115 S. Decesari, M. Paglione, M. Rinaldi, M. Dall'Osto, R. Simó, N. Zanca, F. Volpi, M. C. Facchini, T. Hoffmann, S. Götz, C. J. Kampf, C. O'Dowd, D. Ceburnis, J. Ovadnevaite and E. Tagliavini, *Atmos. Chem. Phys.*, 2020, **20**, 4193–4207.
116 T. H. Bertram, R. E. Cochran, V. H. Grassian and E. A. Stone, *Chem. Soc. Rev.*, 2018, **47**, 2374–2400.
117 R. E. Cochran, O. Laskina, T. Jayarathne, A. Laskin, J. Laskin, P. Lin, C. Sultana, C. Lee, K. A. Moore, C. D. Cappa, T. H. Bertram, K. A. Prather, V. H. Grassian and E. A. Stone, *Environ. Sci. Technol.*, 2016, **50**, 2477–2486.
118 K. A. Prather, T. H. Bertram, V. H. Grassian, G. B. Deane, M. D. Stokes, P. J. DeMott, L. I. Aluwihare, B. P. Palenik, F. Azam, J. H. Seinfeld, R. C. Moffet, M. J. Molina, C. D. Cappa, F. M. Geiger, G. C. Roberts, L. M. Russell, A. P. Ault, J. Baltrusaitis, D. B. Collins, C. E. Corrigan, L. A. Cuadra-Rodriguez, C. J. Ebben, S. D. Forestieri, T. L. Guasco, S. P. Hersey, M. J. Kim, W. F. Lambert, R. L. Modini, W. Mui, B. E. Pedler, M. J. Ruppel, O. S. Ryder, N. G. Schoepp, R. C. Sullivan and D. Zhao, *Proc. Natl. Acad. Sci. U. S. A.*, 2013, **110**, 7550–7555.
119 A. R. J. Nelson and S. W. Prescott, *J. Appl. Crystallogr.*, 2019, **52**, 193–200.
120 M. D. King, K. C. Thompson, T. Arnold, A. R. Rennie, T. W. D. Robson and R. J. L. Welbourn, Oxidation of a bilayer of DOPC by aqueous ozone – a chemical, kinetic and mechanistic investigation, 2018, https://data.isis.stfc.ac.uk/doi/STUDY/103198184/.
121 E. J. Stuckey, R. J. L. Welbourn and M. D. King, Oxidation of a natural organic matter at air-mineral interface by aqueous ozone – a proof of concept, 2022, https://data.isis.stfc.ac.uk/doi/STUDY/115144602/.
122 E. J. Stuckey, R. J. L. Welbourn and M. D. King, Finishing the study of Oxidation of a bilayer of DOPC, POPC and DPPC by aqueous ozone – a chemical, kinetic and mechanistic investigation, 2022, https://data.isis.stfc.ac.uk/doi/STUDY/115144567/.
123 M. D. King, S. H. Jones, A. R. Rennie, K. C. Thompson, A. D. Ward and E. Watkins, Bilayer oxidation using labelled POPC to confirm chemical mechanism and structure of decay by ozone oxidation, 2012, DOI: 10.5291/ILL-DATA.9-10-1241.
124 M. D. King, P. Gutfreund, A. R. Rennie, T. W. D. Robson, A. D. Ward and R. J. L. Welbourn, Oxidation of bilayer of labelled DPPC by aqueous hydroxyl radical; elucidating a mechanism for atmospheric science, 2018, DOI: 10.5291/ILL-DATA.9-10-1517.
125 J. Webster, S. Holt and R. Dalgliesh, *Phys. B*, 2006, **385–386**, 1164–1166.
126 J. R. P. Webster, S. Langridge, R. M. Dalgliesh and T. R. Charlton, *Eur. Phys. J. Plus.*, 2011, **126**, 112.
127 T. R. Charlton, R. L. S. Coleman, R. M. Dalgliesh, C. J. Kinane, C. Neylon, S. Langridge, J. Plomp, N. G. J. Webb and J. R. P. Webster, *Neutron News*, 2011, **22**, 15–18.
128 O. Arnold, J. Bilheux, J. Borreguero, A. Buts, S. Campbell, L. Chapon, M. Doucet, N. Draper, R. Ferraz Leal, M. Gigg, V. Lynch, A. Markvardsen, D. Mikkelson, R. Mikkelson, R. Miller, K. Palmen, P. Parker, G. Passos, T. Perring, P. Peterson, S. Ren, M. Reuter, A. Savici, J. Taylor, R. Taylor, R. Tolchenov, W. Zhou and J. Zikovsky, *Nucl. Instrum. Methods Phys. Res., Sect. A*, 2014, **764**, 156–166.
129 P. Gutfreund, T. Saerbeck, M. A. Gonzalez, E. Pellegrini, M. Laver, C. Dewhurst and R. Cubitt, *J. Appl. Crystallogr.*, 2018, **51**, 606–615.
130 P. S. Pershan, *Phys. Rev. E*, 1994, **50**, 2369–2372.
131 O. S. Heavens, *Rep. Prog. Phys.*, 1960, **23**, 1–65.
132 S. Chiu, E. Jakobsson, S. Subramaniam and H. Scott, *Biophys. J.*, 1999, **77**, 2462–2469.
133 T. K. Lind, M. Cárdenas and H. P. Wacklin, *Langmuir*, 2014, **30**, 7259–7263.
134 H. Bader and J. Hoigné, *Water Res.*, 1981, **15**, 449–456.
135 A. V. Levanov, O. Y. Isaikina, A. N. Tyutyunnik, E. E. Antipenko and V. V. Lunin, *J. Anal. Chem.*, 2016, **71**, 549–553.
136 J. Hoigné, in *The Chemistry of Ozone in Water*, Springer US, 1988, pp. 121–141.
137 K. Bullrich, in *Scattered Radiation in the Atmosphere and the Natural Aerosol*, 1964, pp. 99–260.
138 D. Sinclair and V. K. La Mer, *Chem. Rev.*, 1949, **44**, 245–267.
139 H. Moosmüller, R. Chakrabarty and W. Arnott, *J. Quant. Spectrosc. Radiat. Transf.*, 2009, **110**, 844–878.
140 D. R. Huffman, *Adv. Phys.*, 1977, **26**, 129–230.
141 F. Hoyle and C. Wickramasinghe, *Astrophys. Space Sci.*, 1999, **268**, 249–261.
142 M. Matsumura and M. Seki, *Astrophys. Space Sci.*, 1986, **126**, 155–165.
143 C. F. Bohren and D. R. Huffman, *Absorption and Scattering of Light by Small Particles*, Wiley, 1998.
144 N. V. Voshchinnikov and J. S. Mathis, *Astrophys. J.*, 1999, **526**, 257–264.
145 Z. S. Wu and Y. P. Wang, *Radio Sci.*, 1991, **26**, 1393–1401.
146 S. Kim, J. Chen, T. Cheng, A. Gindulyte, J. He, S. He, Q. Li, B. A. Shoemaker, P. A. Thiessen, B. Yu, L. Zaslavsky,

J. Zhang and E. E. Bolton, *Nucleic Acids Res.*, 2025, **53**, D1516–D1525.
147 I. H. Malitson, *J. Opt. Soc. Am.*, 1965, **55**, 1205.
148 R. H. Shepherd, M. D. King, A. A. Marks, N. Brough and A. D. Ward, *Atmos. Chem. Phys.*, 2018, **18**, 5235–5252.
149 G. M. Hale, *Appl. Opt.*, 1973, **12**, 555–563.
150 P. Laven, *MiePlotv4.6*, 2024.
151 J. M. Haywood and K. P. Shine, *Geophys. Res. Lett.*, 1995, **22**, 603–606.
152 D. J. Delene and J. A. Ogren, *J. Atmos. Sci.*, 2002, **59**, 1135–1150.
153 E. Rudolphi-Skórska, M. Filek and M. Zembala, *J. Membr. Biol.*, 2017, **250**, 493–505.
154 I. O. Bacellar, M. S. Baptista, H. C. Junqueira, M. Wainwright, F. Thalmann, C. M. Marques and A. P. Schroder, *Biochim. Biophys. Acta Biomembr.*, 2018, **1860**, 2366–2373.
155 B. Bagheri, P. Boonnoy, J. Wong-ekkabut and M. Karttunen, *Phys. Chem. Chem. Phys.*, 2023, **25**, 18310–18321.
156 H. L. Smith, M. C. Howland, A. W. Szmodis, Q. Li, L. L. Daemen, A. N. Parikh and J. Majewski, *J. Am. Chem. Soc.*, 2009, **131**, 3631–3638.
157 L. Cwiklik and P. Jungwirth, *Chem. Phys. Lett.*, 2010, **486**, 99–103.
158 M. Lis, A. Wizert, M. Przybylo, M. Langner, J. Swiatek, P. Jungwirth and L. Cwiklik, *Phys. Chem. Chem. Phys.*, 2011, **13**, 17555.
159 K. C. Thompson, S. H. Jones, A. R. Rennie, M. D. King, A. D. Ward, B. R. Hughes, C. O. M. Lucas, R. A. Campbell and A. V. Hughes, *Langmuir*, 2013, **29**, 4594–4602.
160 D. Hu, M. R. Alfarra, K. Szpek, J. M. Langridge, M. I. Cotterell, C. Belcher, I. Rule, Z. Liu, C. Yu, Y. Shao, A. Voliotis, M. Du, B. Smith, G. Smallwood, P. Lobo, D. Liu, J. M. Haywood, H. Coe and J. D. Allan, *Atmos. Chem. Phys.*, 2021, **21**, 16161–16182.
161 D. Hu, M. R. Alfarra, K. Szpek, J. M. Langridge, M. I. Cotterell, M. J. Flynn, Y. Shao, A. Voliotis, M. Du, D. Liu, B. Johnson, G. McFiggans, J. M. Haywood, H. Coe and J. D. Allan, *J. Geophys. Res. Atmos.*, 2023, **128**, e2023JD039178.
162 A. Hartikainen, M. Ihalainen, D. Shukla, M. Rohkamp, A. Mukherjee, Q. He, S. Piel, A. Virkkula, D. Li, T. Kokkola, S. Jeong, H. Koponen, U. Etzien, A. Das, K. Luoma, L. Schwalb, T. Gröger, A. Barth, M. Sklorz, T. Streibel, H. Czech, B. Gündling, M. Kalberer, B. Buchholz, A. Hupfer, T. Adam, T. Hohaus, J. Øvrevik, R. Zimmermann and O. Sippula, *Atmos. Chem. Phys.*, 2025, **25**, 9275–9294.